

Novel ^{18}F -Labeled Radioligands for Positron Emission Tomography Imaging of Myelination in the Central Nervous System

Anand Dev Tiwari,[†] Junqing Zhu,[†] Jingqiang You,[§] Brendan Eck,[‡] Jinle Zhu,[†] Xu Wang,[⊥] Xizhen Wang,^{||} Bin Wang,[⊥] Jerry Silver,[§] David Wilson,[‡] Chunying Wu,^{*,†} and Yanming Wang^{*,†,⊥} 

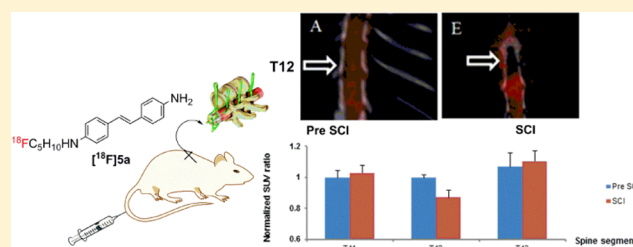
[†]Department of Radiology, [‡]Biomedical Engineering, and [§]Neuroscience, Case Western Reserve University, Cleveland, Ohio 44106, United States

^{||}Department of Radiology, Weifang Medical University, Weifang, Shandong 261053, China

[⊥]Department of Radiology, Binzhou Medical University, Binzhou, Shandong 256603, China

Supporting Information

ABSTRACT: Myelin is the protective sheath that surrounds nerves in vertebrates to protect axons, which thereby facilitates impulse conduction. Damage to myelin is associated with many neurodegenerative diseases such as multiple sclerosis and also includes spinal cord injury (SCI). The small size of the spinal cord poses formidable challenges to *in vivo* monitoring of myelination, which we investigated via conducting a structure–activity relationship study to determine the optimum positron-emitting agent to use for imaging myelin using positron emission tomography (PET). From these studies, [^{18}F]PENDAS was identified as the lead agent to use in conjunction with PET imaging to delineate the integrity of spinal cord myelin. A subsequent *in vivo* PET imaging study of [^{18}F]PENDAS in rats with SCI showed promising pharmacokinetic results that justify further development of imaging markers for diagnosing myelin-related diseases. Additionally, [^{18}F]PENDAS could be valuable in determining the efficacy of therapies that are currently under development.



From these studies, [^{18}F]PENDAS was identified as the lead agent to use in conjunction with PET imaging to delineate the integrity of spinal cord myelin. A subsequent *in vivo* PET imaging study of [^{18}F]PENDAS in rats with SCI showed promising pharmacokinetic results that justify further development of imaging markers for diagnosing myelin-related diseases. Additionally, [^{18}F]PENDAS could be valuable in determining the efficacy of therapies that are currently under development.

INTRODUCTION

Spinal cord injury (SCI) is one of the most catastrophic traumas to the body that affects 250 000–500 000 people worldwide annually. A traumatic blow to the spinal cord typically crushes the nerve fibers, which causes apoptosis of oligodendrocytes and subsequent loss of myelin.¹ Diagnosis, prognosis, and efficacy evaluation of SCI treatments require imaging tools that permit the detection and quantification of myelin status that correlates with the degree of physical disability.

In the clinic, SCI is primarily assessed through magnetic resonance imaging (MRI), which is a nonspecific imaging modality that only detects overall lesion load in the spinal cord; however, specific myelin changes from onset to late stage have important implications for diagnosis and prognosis. This is particularly true in SCI where myelopathy becomes the primary characteristic of clinical presentation with extensive abnormalities in the spinal cord. It is thus critical to detect and quantify the extent of demyelination and remyelination and elucidate their relationship with physical disability.

At present, most of the available drugs for treating SCI decrease inflammation through modulation of the immune system. New myelin repair therapies are currently under development that are designed to promote remyelination.^{2,3} A new approach to SCI therapy is that myelin repair can be done via transplanting myelinated stem cells^{4–6} and/or antibody⁷

approaches, which may be more effective in reducing long-term disability.⁸

For accurate diagnosis and evaluation of myelin repair therapies, it is critical to develop a molecular imaging tool that allows for direct detection and quantification of myelin changes in the spinal cord. Because MRI signals only reflect changes in tissue water content that do not distinguish myelin damage from inflammation or edema, conventional T_2 -weighted MRI lacks pathological specificity. Other types of more technically sophisticated MR imaging methods such as fluid-attenuated inversion recovery and diffusion tensor MR imaging are also nonspecific in detecting changes in myelin. Recently, an MRI technique using magnetization transfer ratio has also been explored to monitor myelin change.⁹ However, this technique still does not provide sensitive and quantitative measures of myelin but can only be used as an indirect measure of myelin integrity.^{10–12}

To address this challenge of myelin imaging in the spinal cord, we set out to employ positron emission tomography (PET) imaging, a widely used clinical imaging modality that has extremely high sensitivity as well as quantitation capability. To optimize the advantages of PET, we synthesized a series of small molecular probes (SMPs) with myelin-binding capability. Some

Received: August 30, 2018

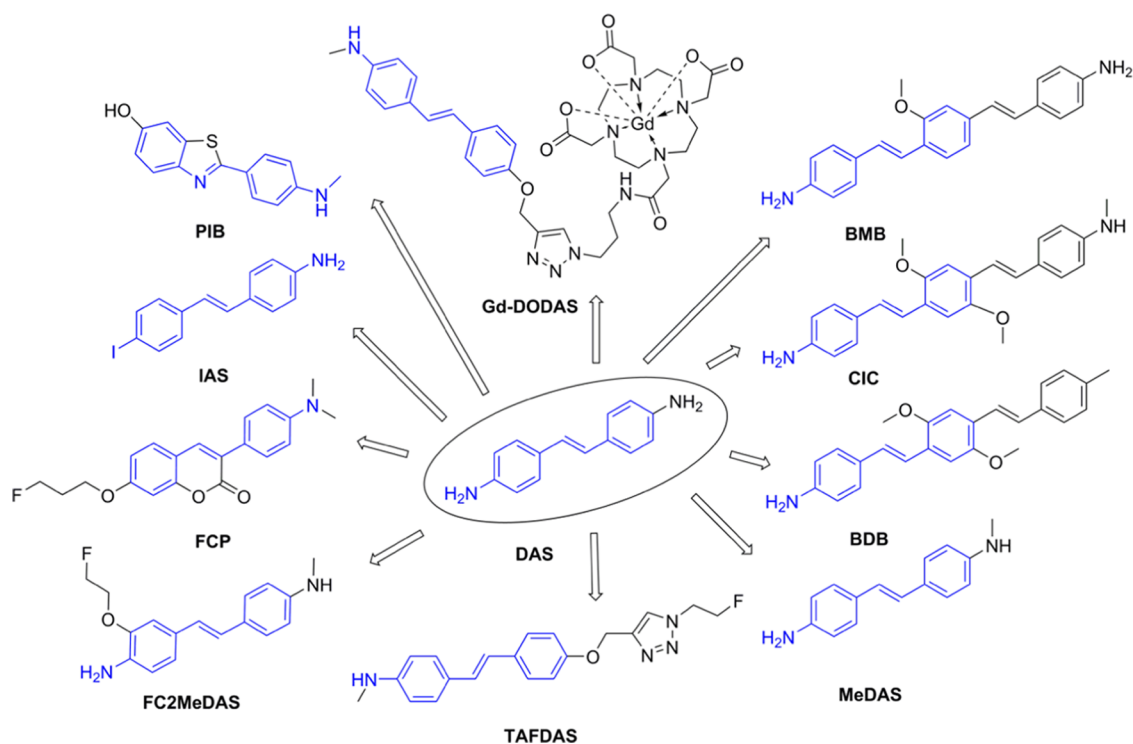


Figure 1. Structures of myelin-imaging agents that have been developed based on stilbene.

of the SMPs can be readily radiolabeled with positron emitters such as C-11 or F-18 that enable us to apply PET to detect and quantify myelin integrity in the central nervous system (CNS).¹³ Subsequent imaging studies showed that these SMPs primarily labeled with C-11 bind with high affinity and specificity to myelin *in vivo* and can be used as an imaging marker to efficaciously evaluate myelin repair therapy in the spinal cord.

In addition to developing a series of myelin-imaging agents for PET imaging, we have also developed agents that can be used in conjunction with single-photon emission computed tomography, MRI, and optical imaging (Figure 1).^{14–25} Among these probes, methyl diamino stilbene (MeDAS), case imaging compound (CIC), myelin-binding agent (BMB), (*E*)-4-(4-amino-3-(2-fluoroethoxy)styryl)-*N*-methylaniline (FC2MeDAS), and triazole fluorinated diamino stilbene (TAFDAS) were radiolabeled and successfully used with PET imaging with a variety of animal models.^{14–19,26,27} Most of these imaging agents share a common diamino stilbene (DAS) pharmacophore, which facilitates specific interaction with myelin sheets. The planar structure of DAS makes it possible to bind to the unique β -sheet assembly present in myelin basic protein (MBP).²⁴ The exact binding mechanism is still unknown due to the complex composition of myelin.

Our previous studies focused on C-11 labeled radiotracers such as BMB, CIC, and MeDAS for *in vivo* PET imaging of myelin to take advantage of its relatively short half-life and predictable radiostability after radiolabeling.^{14,16,18} Completion of these studies provided proof of principle that SMPs can be developed for PET imaging of myelin and used for efficacy evaluation of remyelination therapies. Thus far, we have identified [¹¹C]MeDAS as a lead PET radiotracer to monitor changes of myelin in the spinal cord. To extend the availability of these agents to a wider audience of users, we developed a series of MeDAS analogues radiolabeled with fluorine-18, which has a significantly longer half-life and therefore would permit remote

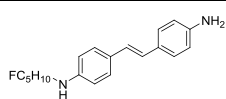
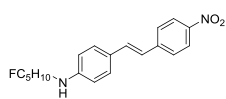
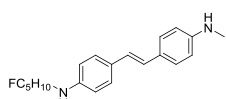
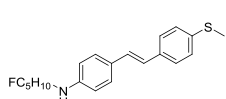
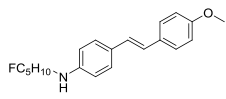
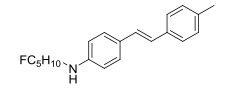
distribution to imaging facilities without onsite cyclotrons. We first developed a series of [¹⁸F]MeDAS analogues such as FC2MeDAS, as shown in [¹⁸F]MeDAS analogues such as FC2MeDAS, as shown in Figure 1.²⁷

To further optimize the *in vivo* properties and pharmacokinetics in the spinal cord, we designed a novel series of fluorinated MeDAS analogues by direct alkylation of one of the amino groups of DAS. After synthesis and radiolabeling, the binding properties and pharmacokinetics of these fluorinated stilbene analogues with different terminal functional groups were evaluated through systematic structure–activity relationship (SAR) studies, which enabled us to identify a novel radiotracer that is ideally suited to ascertain myelin integrity via clinical PET imaging.

RESULTS

Chemistry. For SAR studies, a series of stilbene derivatives was designed and synthesized, as shown in Table 1. Based on [¹¹C]MeDAS, a C-11 labeled radioligand,^{18,28} we introduced *N*-1-fluoropentyl amino groups to a series of stilbene analogues containing $-\text{NH}_2$, $-\text{NO}_2$, $-\text{NHCH}_3$, $-\text{OCH}_3$, $-\text{SCH}_3$, and $-\text{CH}_3$ functional groups. In addition, a fluoropentyl chain was selected based on SAR studies, as previously described in *J. Med. Chem.* 2016, 59, 3705–3718. In that study, we tested a series of compounds with various lengths of fluoroalkyl groups. SAR studies suggested that longer fluoroalkyl groups such as fluoroethoxyethoxy showed optimal lipophilicity and radiochemical stability. Fluoropentyl has length similar to fluoroethoxyethoxy and is widely used in other fluorinated agents for PET imaging, such as [¹⁸F]-2-(5-fluoropentyl)-2-methyl malonic acid for cancer imaging,²⁹ [¹⁸F]-(fluoropentyl)-triphenylphosphonium salt for myocardial imaging,³⁰ and [¹⁸F]3-(4,5-dihydrooxazol-2-yl)phenyl (5-fluoropentyl)-carbamate for neuroimaging.³¹ We thus selected fluoropentyl to introduce F-18 to myelin-imaging derivatives.

Table 1. List of the Final Compounds (5a–f) with Their Calculated log *P* (clog *P*)

Entry	Structure	clog <i>P</i>
5a		4.10
5b		5.50
5c		4.40
5d		5.33
5e		4.76
5f		5.38

The lipophilicity in terms of log *P* of the newly designed compounds was estimated to be in the range of 4.1–5.3 using ChemDraw professional 15.0, as listed in Table 1. This range of lipophilicity is considered high enough to be CNS-permeable, which thus warrants subsequent synthesis and investigation to image myelin *in vivo*.

The synthesis of these novel compounds is shown in Scheme 1. Starting with diethyl (4-aminobenzyl)phosphonate (1), Boc was used to protect the amino group to generate *tert*-butyl (4-((diethoxyphosphoryl)methyl)phenyl)-carbamate (2) in 95% yield, which was followed by alkylation with 1-bromo-5-fluoropentane to obtain *tert*-butyl (4-((diethoxyphosphoryl)methyl)phenyl)(5-fluoropentyl)-carbamate (3) in 43% yield. Compound 3 was then coupled with 4-substituted benzaldehyde (a–f) through the Horner–Wadsworth–Emmons reaction to produce intermediates 4a–f in 50–90% yield. A one-pot reaction was then done using SnCl₂ in methanol and ethyl acetate for 4a and HCl (1.2 M) for 4b–f, which allowed for reduction of the nitro group to the amino group and simultaneous deprotection of the Boc group in 50–90% yield to generate the final products 5a–f, which were used as radiochemical synthesis standards and for biological studies.^{23,27}

For the radiosynthesis of [¹⁸F]5a, the ditosylated compound 7 was prepared from 1,5-diol pentane (6) in 65% yield. As shown in Scheme 2, the Boc-protected amine of compound 2 was alkylated in DMF and NaH (60%) to obtain tosylated compound 8 in 32% yield. The Boc-protected-*N*-pentane-tosylated diethyl benzylphosphonate (8) was coupled with 4-

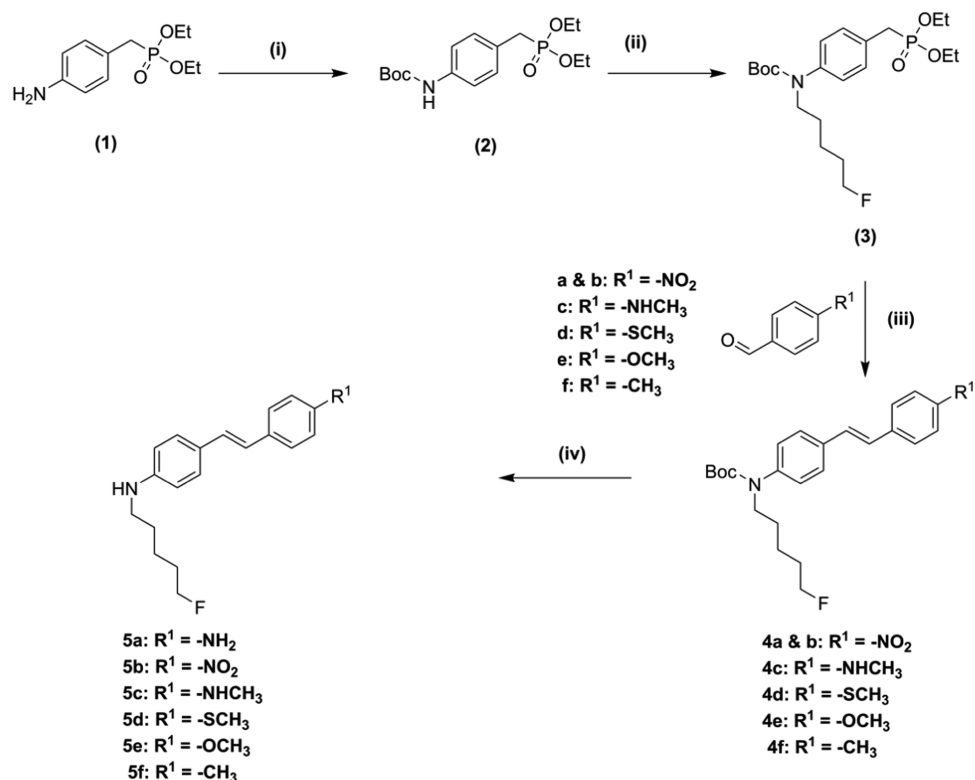
nitrobenzaldehyde (a) to produce the precursor (9a) through the Horner–Wadsworth–Emmons reaction in 40% yield. This precursor (9a) was used for the radiosynthesis of ¹⁸F-labeled 5a for *in vivo* microPET/computerized tomography (CT) studies.

We then systematically evaluated these newly synthesized fluorinated stilbene derivatives (5a–f) *in vitro* as well as *in vivo* and *ex vivo* to determine their properties of binding to myelin. The UV absorption and excitation/emission spectra of all of the final products (~1 mM) were first acquired in acetonitrile (MeCN), as shown in Figures 2 and 3, respectively. The absorption wavelengths ranging from 340 to 425 nm were observed for the final compounds (5a–f). The excitation wavelengths ranging from 350 to 410 nm and emission wavelengths ranging from 415 to 575 nm were determined for all the test compounds (5a–f). Such wavelengths render these compounds highly fluorescent and suitable for fluorescent tissue staining to evaluate the myelin-binding properties *in vitro* or *ex vivo*.

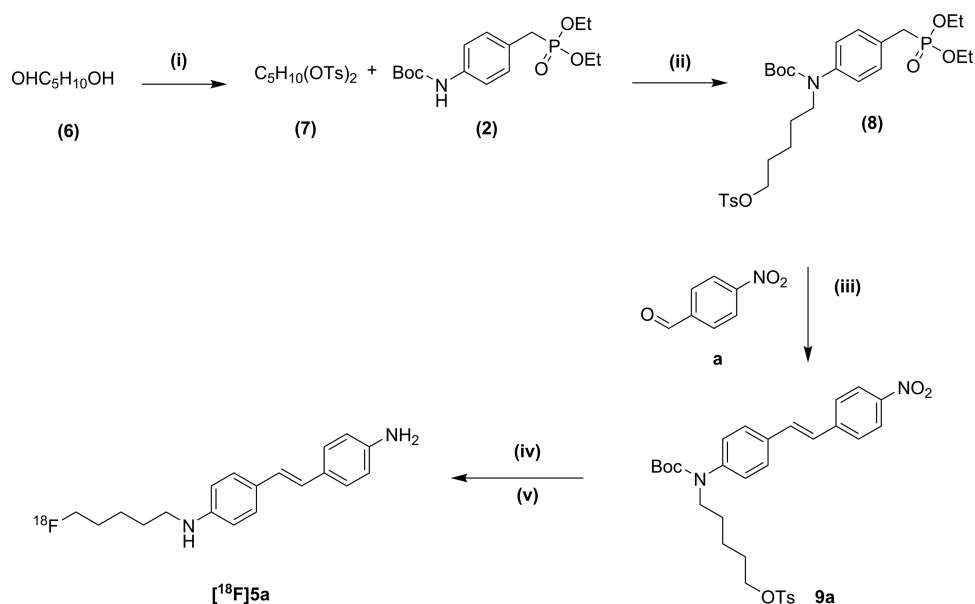
In Vitro Fluorescent Tissue Staining. We first conducted *in vitro* fluorescent tissue staining to evaluate the myelin-binding properties of the newly synthesized compounds. Figure 4A illustrates that compounds 5a–f stained the myelinated regions, including the corpus callosum and striatum, where the fluorescent intensity correlated with the myelin distribution pattern in the brain. To quantitatively compare myelin-binding potentials, the test compounds were screened *in vitro* in mouse brain tissue sections at the same concentration (1 mM) for 25 min, and tissue sections were imaged under a microscope (Leica DM4000B) at the same exposure time. After staining, we defined two standard regions of interest (ROIs), one from the genu corpus callosum (gcc) that is myelin-rich and the other from the subcortical gray matter (cortex) that is myelin-deficient. These differences are illustrated in Figure 4A, from which the fluorescent intensity was calculated to determine the fluorescence intensity ratios (FIRs) between the two ROIs (Figure 4B). As a result, compounds 5a and 5c show the highest FIR values >1.2 among all of the newly synthesized compounds (Table 1). This SAR study suggests that compounds 5a and 5c exhibit high *in vitro* binding specificity, justifying them as lead candidates for subsequent *ex vivo* evaluation.

Ex Vivo Imaging of the Spinal Cord and Brain. To determine if the lead compounds bind to myelin of the spinal cord and enter the brain, we conducted *ex vivo* staining studies. Thus, 5a and 5c with a dose of 40 mg/kg were administered via tail vein injection to wild-type (WT) mice; 30–60 min after the injection, the mice were perfused with saline followed by 4% paraformaldehyde (PFA) and their brains and spinal cords were then dissected and sectioned. Figure 5 illustrates that the two lead compounds (5a and 5c) readily entered the brain and specifically bound to myelin-rich areas of the white matter regions such as the corpus callosum and striatum. Direct comparison of fluorescent intensity, albeit qualitative, showed that such *in situ* staining with compound 5a (Figure 5A,B) is higher than with compound 5c (Figure 5C,D).

In Vitro Tissue Staining of Focal Demyelination. Based on the selective staining of 5a *in situ* in white matter regions, we further evaluated the capability of compound 5a to detect myelin changes in a rat model in which demyelination was induced by injections of lysolethicin unilaterally into the corpus callosum to generate a focal demyelinated lesion. As shown in Figure 5E, the presence of demyelinated foci was readily detected following fluorescent staining of the brain tissue sections with compound 5a, which was subsequently verified

Scheme 1. Synthesis of [^{19}F]- C_5H_{10} -DAS Analogues^a

^aReagents and conditions: (i) $(\text{Boc})_2\text{O}$, tetrahydrofuran (THF)/ H_2O (3:1); 20 °C; 24 h; yield, 95%. (ii) NaH(60%); dimethylformamide (DMF); 0 °C; 12 h; yield, 43%. (iii) NaH(60%); DMF; 0 °C; 4 h; yield, 40–80%. (iv) SnCl_2/HCl (1.2 M); 70 °C; 6 h; yield, 60–90%.

Scheme 2. Radiosynthesis of [^{18}F]5a^a

^aReagents and conditions: (i) TsCl, dichloromethane (DCM); 20–0 °C; 12 h; yield, 65%. (ii) THF; NaH (60%); DMF; 0 °C; 6 h; yield, 32%. (iii) THF (60%); DMF; 0 °C; 4 h; yield, 40%. (iv) [^{18}F]fluoride ion; K_{222} ; K_2CO_3 ; MeCN; yield, 60%. (v) SnCl_2 ; EtOH; HCl; NaOH; yield, 40%.

using conventional luxol fast blue (LFB) and cresyl violet staining in adjacent sections (Figure 5F).¹⁶

Radiosynthesis. The preceding results from the in vitro and ex vivo studies encouraged us to evaluate compound 5a for the in vivo pharmacokinetics profile after labeling with the positron emitter fluorine-18. A nucleophilic substitution reaction with

fluorine-18 generated by an onsite cyclotron was used to conduct the radiosynthesis. As shown in Scheme 2, a tosylated precursor (9a) was first synthesized and subsequently used for nucleophilic substitution reaction with [^{18}F]KF in the presence of K_2CO_3 and kryptofix (K_{222}) in MeCN at 115 °C for 10 min. Purification of the fluorinated intermediate to remove unreacted

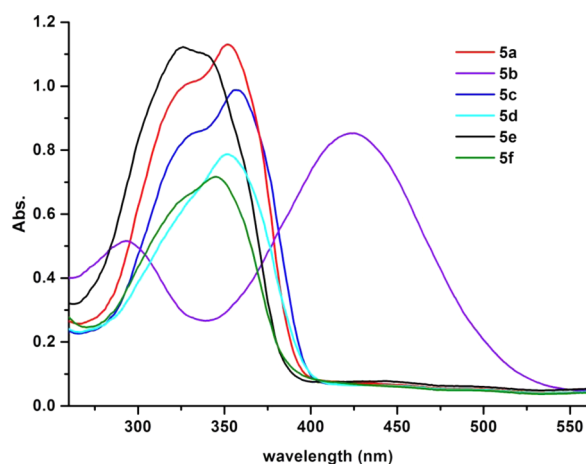


Figure 2. UV absorption spectra of compounds 5a–f.

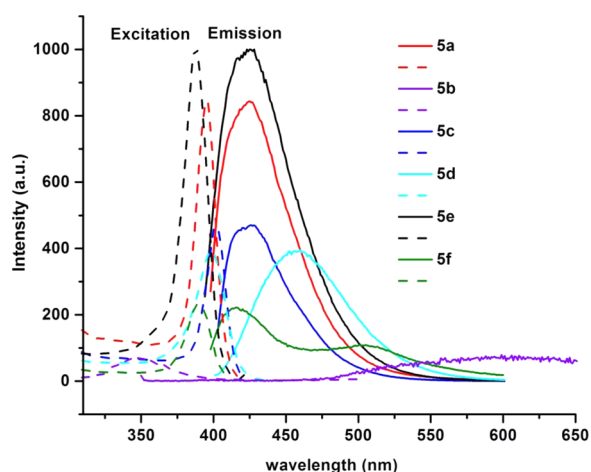


Figure 3. Fluorescence emission and excitation spectra for compounds 5a–f in acetonitrile (1 mM) solution.

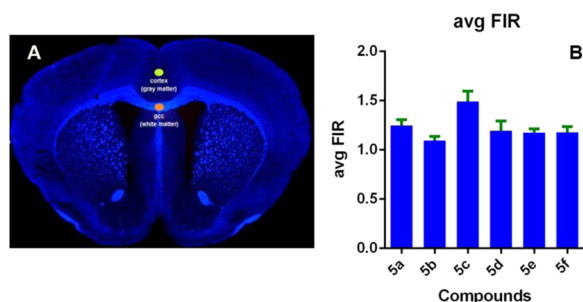


Figure 4. FIR in white matter vs gray matter. (A) Representative in vitro tissue staining showing ROI used for calculation of FIR for white matter and gray matter. (B) ImageJ used to calculate FIR of each target compound (5a–f). For each compound, $n = 15$ sections were used.

free fluorine-18 was done by passing through a silica Sep-Pak. The 4-nitro group of the F-18-labeled intermediate was then reduced by SnCl_2 in ethanol (EtOH) at 120°C for 10 min, followed by acid hydrolysis to cleave the Boc group to yield the primary amine ($[^{18}\text{F}]\mathbf{5a}$). The reaction mixture was cooled to room temperature, and the pH was adjusted to 8–9 by addition of sodium hydroxide (NaOH, 1.0 M, 0.5 mL), which was followed by purification through semipreparative high-performance liquid chromatography (HPLC) to yield the pure product $[^{18}\text{F}]\mathbf{5a}$ with a modest yield of 40%.³² The identity and purity of

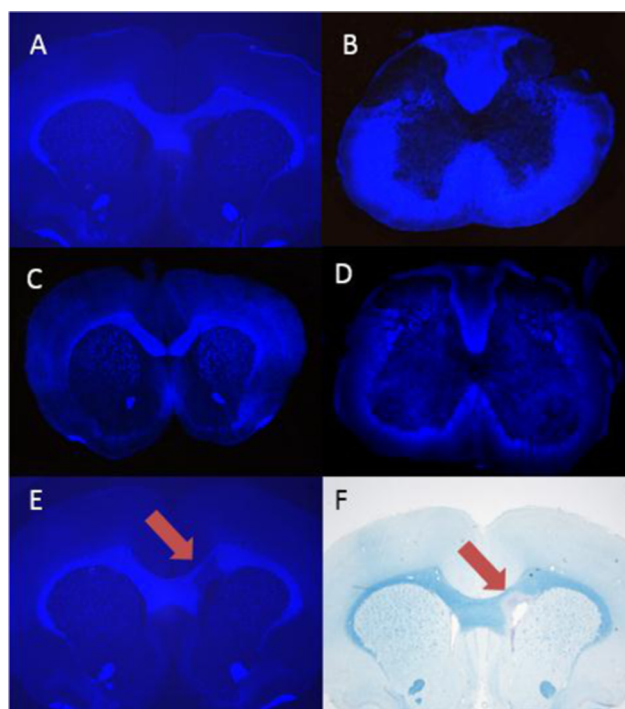


Figure 5. Ex vivo staining of whole brain and spinal cord tissue sections with compounds (A, B) 5a and (C, D) 5c. In vitro compound 5a (E) staining of whole brain tissue section from lysophosphatidylcholine (LPC)-treated rat that is consistent with luxol fast blue (LFB) staining in adjacent tissue section (F); demyelinated lesions are shown by the arrow.

the final compound was determined via HPLC by co-injection of the compound with a nonradioactive standard. Analytical radio-HPLC was used to determine the radiochemical purity (RCP) of the final product, which was >98%. The molar activity (A_m) at the end of synthesis was $92.5\text{ GBq}/\mu\text{mol}$.

In Vitro Autoradiography. Following radiolabeling with F-18, we conducted autoradiography of mouse brain tissue sections using compound $[^{18}\text{F}]\mathbf{5a}$. Thus, fresh frozen mouse brain sections were incubated with $[^{18}\text{F}]\mathbf{5a}$ ($2\ \mu\text{Ci}$, 5% ethanol in phosphate-buffered saline (PBS)). From Figure 6A, it is evident that distinct labeling of the corpus callosum was observed after mouse brain sections were exposed to $[^{18}\text{F}]\mathbf{5a}$ for 20 min, which indicates that the autoradiographic results correlate with the histological staining results of the myelinated region. To further illustrate the binding specificity of $[^{18}\text{F}]\mathbf{5a}$

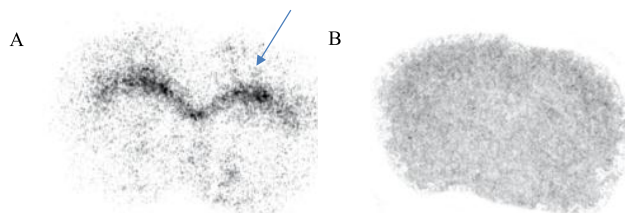


Figure 6. In vitro film autoradiography. (A) Specific binding of $[^{18}\text{F}]\mathbf{5a}$ to the myelinated corpus callosum in the mouse brain (coronal). The arrows show myelinated corpus callosum labeled by $[^{18}\text{F}]\mathbf{5a}$. (B) No distinct autoradiographic visualization of the corpus callosum was observed after pretreatment of the mouse sections ($n = 5$) with unlabeled MeDAS (1 mM), indicating that $[^{18}\text{F}]\mathbf{5a}$ binds to myelinated corpus callosum with high selectivity and specificity.

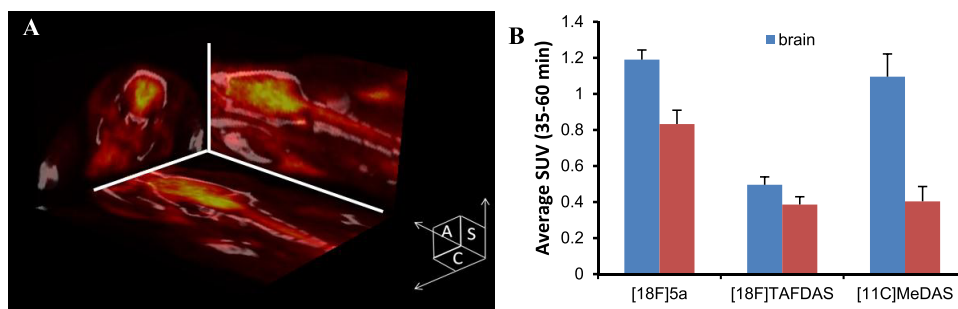


Figure 7. (A) Three-dimensional box representation of (A) axial, (S) sagittal, and (C) coronal microPET/CT images of a rat brain and cervical spinal cord following intravenous (i.v.) administration of [¹⁸F]5a, showing high uptake in the myelin-rich white matter regions of the brain and spinal cord ($n = 3$). (B) Comparison of [¹⁸F]5a uptake in WT rat brain and spinal cord with previously developed [¹⁸F]TAFDAS and [¹¹C]MeDAS, showing relatively higher uptake in the brain compared to [¹¹C]MeDAS and significantly higher uptake in spinal cord than with [¹⁸F]TAFDAS and [¹¹C]MeDAS at later time points.

toward myelin, fresh frozen mouse brain sections were incubated with excess MeDAS, a compound that binds to myelin with high specificity. After 10 min, [¹⁸F]5a (2 μ Ci, 5% ethanol in PBS) was added to the above solution and the brain sections were allowed to incubate for another 20 min. As shown in Figure 6B, pretreatment of the sections with an excess amount of MeDAS significantly reduced the autoradiographic labeling of the corpus callosum. After 20 min exposure to [¹⁸F]5a, no distinct labeling of corpus callosum was observed, indicating that [¹⁸F]5a binds to myelinated corpus callosum with high specificity.

Quantitative MicroPET/CT Imaging of Myelin in the Brain. Post-radiolabeling, we obtained the pharmacokinetic profile of [¹⁸F]5a in the brain of Sprague-Dawley (SD) rats ($n = 3$). Quantitative analysis required registering microPET images to the CT images, as shown in Figure 7A in a three-dimensional (3D) presentation of axial, coronal, and sagittal views to define ROIs accurately and to quantify the radioactivity concentration of [¹⁸F]5a. The in vivo radioactivity concentration was evaluated in terms of average standardized uptake value (SUV) in the spinal cord and brain. [¹⁸F]5a showed high initial uptake in the brain, which peaked at 1 min post-injection and was followed by rapid clearance before reaching a stable plateau at 20 min post-injection. This profile suggests that [¹⁸F]5a is a promising myelin-imaging radioligand with high brain permeability and binding affinity for myelin. As shown in Figure 7B, compared to previously developed [¹⁸F]TAFDAS and [¹¹C]MeDAS, [¹⁸F]5a exhibited the highest uptake in the spinal cord, and the uptake of [¹⁸F]5a in the brain was similar to C-11-labeled [¹¹C]MeDAS but significantly higher than [¹⁸F]TAFDAS at later time points.

The in vivo binding specificity of [¹⁸F]5a was further evaluated by investigating the pharmacokinetic profiles of [¹⁸F]5a in a shiverer mouse model that is myelin-deficient in the brain. For direct comparison, both shiverer mice and their age-matched littermates were imaged side by side in a PET/CT scanner. After [¹⁸F]5a was administered, dynamic emission scans were immediately acquired for 60 min in 3D list mode. The brain uptake of [¹⁸F]5a was quantified after co-registration of PET images with CT images. The radioactivity in terms of percent of injected dose (%ID) between 35 and 60 min was summed and compared after the brain concentration of [¹⁸F]5a reached a plateau. As shown in Figure 8, the average uptake (35–60 min) of [¹⁸F]5a in the shiverer mouse brain was $10.87 \pm 0.72\%$ ID/g, which was significantly decreased compared to the control littermates ($19.39 \pm 1.50\%$ ID/g, $p = 0.0416$, two-tailed t test).

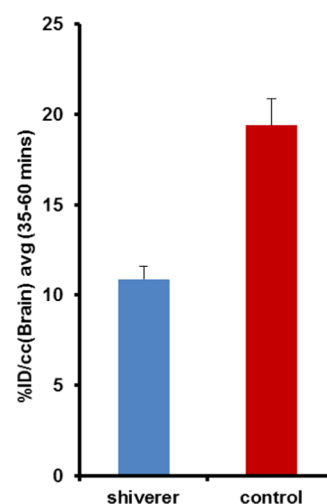


Figure 8. Average brain uptake of [¹⁸F]5a between 35 and 60 min post-injection in shiverer mice (blue) and age-matched control (red) ($p = 0.0416$, two-tailed t test).

Ex Vivo Three-Dimensional Cryofluorescence Imaging. To further validate the in vivo PET imaging results, we conducted ex vivo 3D cryofluorescence imaging of the rat spinal cord in the same animals following [¹⁸F]5a-PET/CT scans. Thus, sequential slices (100 μ m thickness) of rat spinal cord were first obtained with a cryo-microtome 30 min after tail vein injection of compound 5a after the [¹⁸F]5a-PET/CT scan. Fluorescent images were then captured at 10 μ m pixel resolution with a fluorescence microscope (Leica DM4000B, Leica Microsystems Inc, Buffalo Grove, IL) to generate an image volume composed of the stacked sequential slices. Misalignment in Cryo-3D images was reduced by aligning sequential slices with control point registration and a rigid-body transformation in Matlab. The Cryo-3D image stack was then visualized using the Amira software package and aligned with microPET/CT images (Figure 9). Cryo-3D provides high-resolution ex vivo data, which could be analyzed from multiple views and color map representations (Figure 10).

Quantitative MicroPET/CT Imaging Studies in the Spinal Cord. The aforementioned studies of [¹⁸F]5a PET/CT imaging of myelin in the brain were followed by conducting [¹⁸F]5a PET/CT imaging of the spinal cord in a rat model of SCI, which involved making a contusion of the spine at thoracic region T12 to introduce demyelination. A baseline scan prior to and 1 day after the contusion was done with [¹⁸F]5a PET

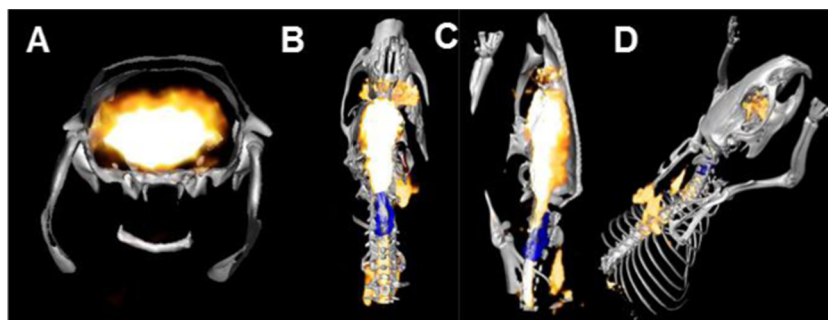


Figure 9. MicroPET/CT/Cryo-3D fluorescence co-registered images: (A) axial, (B) coronal, (C) sagittal, and (D) 3D view of the rat brain and spinal cord following intravenous administration of [^{18}F]5a showing high uptake in the myelin-rich white matter region of the brain. Cryo-3D fluorescence is shown in the T1–13 region of the spinal cord.

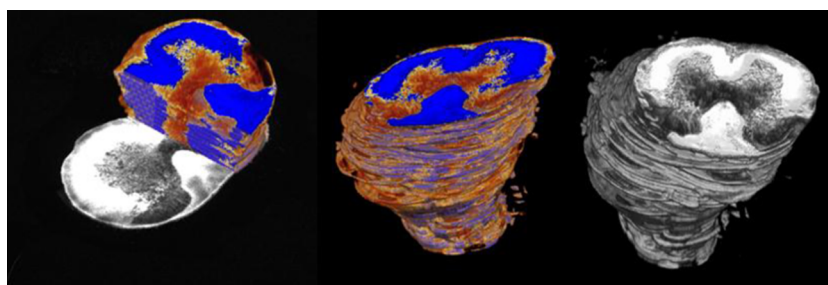


Figure 10. Ex vivo cryogenic 3D images of axial and sagittal views and color map processed with Amira for the spinal cord sections ($n = 5$) using compound 5a.

imaging. [^{18}F]5a uptake in four spine segments (T10–13) was determined and normalized to the average (T10–13) spine uptake. As shown in Figure 11A,B, the intact thoracic region of

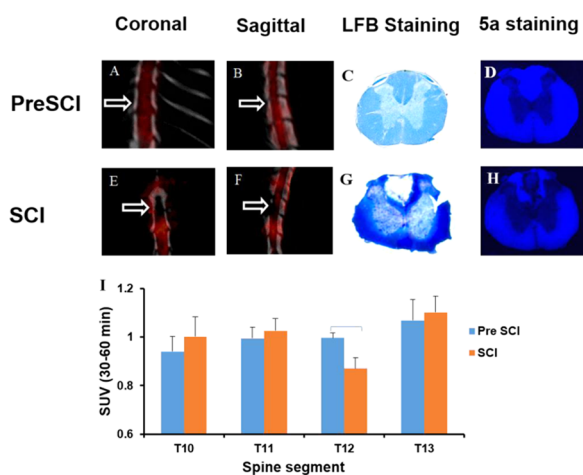


Figure 11. Representative PET/CT fusion images in rats acquired before SCI surgery (baseline scan) with higher-magnification coronal (A) and sagittal (B) images in the T12 spinal cord. Representative PET/CT fusion images in rats acquired 1 day after SCI surgery with higher-magnification coronal (E) and sagittal (F) images in the T12 spinal cord. Note the decreased signal contrast in the SCI animal ($n = 3$) compared to the baseline scan. In situ histological staining of the SCI (T12) tissue section with reference compound 5a after microPET/CT imaging showing a demyelinated lesion at the dorsal portion (H), which is consistent with LFB staining using adjacent sections (G). (I) Quantification of the total cumulative [^{18}F]5a uptake in the T10–13 in terms of normalized SUV ratio at 30–60 min post-injection showing significantly lower uptake in the SCI (T12) compared to that in baseline scans.

the spinal cord before contusion was clearly visualized by [^{18}F]5a PET imaging. After contusion, the lesion at vertebrae level T12 was readily detected by [^{18}F]5a PET (compare Figure 11E,F). Figure 11E illustrates that the uptake of [^{18}F]5a in T12 in the SCI group was 0.86, which was significantly lower than that in the baseline scans (1.00). Post-microPET/CT imaging, demyelination in the lesion region was verified by in situ histological staining. As shown in Figure 11F–H, 30 min after injection of nonlabeled compound 5a through the tail vein, no staining was observed in the dorsal column after contusion, which was further verified by LFB and cresyl violet staining.

DISCUSSION AND CONCLUSIONS

Discovery and development of drugs for biomedical imaging represent a new frontier in medicinal chemistry. Compared to therapeutic drugs, imaging drugs are used in much smaller quantities, at least 1000-fold less than therapeutic drugs. Consequently, imaging drugs require less rigorous toxicity testing but more stringent requirements for target-binding specificity, in vivo pharmacokinetic properties, and metabolic activities. Probably the most distinctively important aspect in imaging drug development lies in the structural design of each particular imaging modality even for imaging the same target. Each different imaging modality requires a specific signaling element and thus distinctive structural design.

In this work, we took a distinct approach to structural design and development of a new class of myelin-imaging agents that are compatible with PET imaging and 3D cryoimaging. The two imaging modalities complement each other, i.e., PET can be used to detect and quantify myelin distribution in vivo, whereas 3D cryoimaging can be used to characterize microscopically the myelin histology in vitro. Since both imaging modalities are tomographic, PET images and 3D cryoimages can be co-registered for cross-referencing and validation. This requires use

of a structurally identical myelin-imaging agent for both imaging modalities.

For this reason, we designed and synthesized a series of stilbene derivatives that are capable of radiolabeling with F-18 for PET and fluorescent staining for 3D cryoimaging. For SAR studies, we first focused on lipophilicity, which is an important physicochemical property for both histochemical staining and in vivo pharmacokinetics in the CNS. A total of six compounds were then designed by introducing NO₂, CH₃, SCH₃, OCH₃, NHCH₃, and NH₂ to one phenyl ring and fluoropentyl amino to the other phenyl ring of stilbene. Following synthesis, the lipophilicity varies as different functional groups were introduced to one of the phenyl rings, which decreases in the order NO₂, CH₃, SCH₃, OCH₃, NHCH₃, and NH₂. For permeability across the blood–CNS barrier, myelin-imaging agents ought to exhibit moderate lipophilicity. But high lipophilicity often results in high nonspecific binding.

In addition, the fluorescent properties of these compounds were also characterized, which is shown in Figure 3. The compounds are all seen to be fluorescent with absorption and excitation wavelengths of ~400 nm. Among all of the compounds tested, compounds 5a and 5e showed the highest fluorescent intensity. Subsequent in vitro fluorescent tissue staining was then conducted to further evaluate the test compounds. For quantitative SAR studies, an FIR was defined between the fluorescent intensity in a myelin-rich genu corpus callosum region and a myelin-deficient subcortical gray matter region. The higher FIR suggests high binding specificity and vice versa. As shown in Figure 4, compounds 5a and 5c showed the highest FIR values among all of the test compounds. These in vitro studies led us to identify compounds 5a, 5c, and 5e as lead compounds. Considering that the lipophilicity of compound 5e is abnormally high, compounds 5a and 5c were thus selected for downstream ex vitro and in vivo studies.

Thanks to the fluorescence exhibited by compounds 5a and 5c, we were able to first evaluate the spinal cord and brain uptake and binding specificity for myelin. After tail vein injection, both compounds readily entered the brain and selectively bound to myelin in the brain and spinal cord. Interestingly, even though both compounds have similar cLogP values, compound 5a displayed potent staining with higher fluorescent intensity than compound 5c, as shown in Figure 5A–D. These in vitro and ex vivo studies suggest that all of the test compounds bind selectively to myelin in the presence of other proteins at the tissue level. This class of compounds binds to myelin not through lipid–lipid interaction but rather through molecular interaction, although the exact binding mechanism has not been defined and needs to be further investigated. As a result, compound 5a could readily detect myelin-damaged lesions induced by lysophosphatidylcholine (LPC) in a rat model, as shown in Figure 5E,F. In addition, following tail vein injection of either nonlabeled compound 5a at a dose as high as 40 mg/kg, no sign of acute toxicity in rats was observed.

The aforementioned studies prompted us to further investigate compound 5a as a radiotracer for PET imaging of myelin. Following radiolabeling with F-18, we tested [¹⁸F]5a in two animal models. PET imaging was first conducted in rats showing [¹⁸F]5a readily entered the spinal cord and brain. The uptake was significantly higher than that of previously developed myelin-imaging agents such as MeDAS and TAFDAS. To determine the binding specificity for myelin in vivo, [¹⁸F]5a was further evaluated in the shiverer mouse model. Compared to age-matched control littermates, brain uptake in myelin-

deficient shiverer mice decreased significantly. Thus, high binding specificity for myelin was observed in vitro, ex vivo, and in vivo in a series of studies showing either labeled or nonlabeled 5a bound selectively to myelin in the presence of other proteins at the tissue level. In addition, following tail vein injection of [¹⁸F]5a, no sign of acute toxicity in rats was observed. These studies suggest that [¹⁸F]5a can be used to detect myelin changes in the brain.

Following PET studies, histological analysis is required to validate the imaging results. Conventional immunohistochemistry is often conducted in selected tissue sections, which is limited to analysis of small fragments of the brain and spinal cord and is inherently biased due to the limited scope of sampling. Three-dimensional cryoimaging, on the other hand, provides a tomographical characterization of the whole tissue of interest and thus is similar to PET imaging. The 3D cryoimaging results are therefore less subjective than conventional immunohistochemistry as sampling bias is essentially eliminated. In addition, thanks to the inherent fluorescence of compound 5a and its optimal pharmacokinetics, histological 3D cryoimaging can also be conducted in situ, which provides the same tomographical characterization of myelin distribution at a microscopic resolution that can be co-registered with PET images for precise validation of the PET imaging results, as shown in Figures 9 and 10. Finally, the imaging sensitivity and specificity of [¹⁸F]5a-PET was ultimately determined in an SCI model with focal demyelination (Figure 11). After contusion at vertebrae level T12, the uptake of [¹⁸F]5a was significantly decreased compared to the baseline scan due to myelin damage, which was further confirmed by in situ staining and histochemistry by LFB and cresyl violet staining.

In summary, a multimodal approach combining in vivo PET and ex vivo 3D cryoimaging has been developed for optimizing the selection of novel F-18-labeled radioligands for imaging myelin. Following the design and synthesis of a series of aminopentyl-fluorinated stilbene derivatives, SAR studies were conducted for characterization and optimization of in vitro and ex vivo binding properties, which led to identification of a lead compound 5a that selectively binds to myelin and readily enters the brain and spinal cord. Subsequent in vivo PET imaging studies in a rat model of contusive SCI showed that [¹⁸F]5a-PET can readily detect myelin damage in the spinal cord, which suggests that [¹⁸F]5a is a potentially valuable PET imaging agent for monitoring myelin changes in the CNS.

EXPERIMENTAL SECTION

General Procedures. All chemicals and reagents were used as received without further purification. Glassware was dried in an oven at 130 °C and purged with dry air before use. Unless otherwise mentioned, reactions were performed open to air. The reactions were monitored by thin-layer chromatography (TLC) and monitored by a dual short-/long-wavelength UV lamp. Flash column chromatography was performed using 230–400 mesh silica gel (Fisher). Nuclear magnetic resonance (NMR) spectra were recorded on a Varian INOVA 400 spectrometer and a 500 MHz Bruker Ascend Avance III HD at room temperature. Chemical shifts for ¹H, ¹³C, and ¹⁹F NMR spectra were reported as δ, parts per million, and referenced to an internal deuterated solvent central line. Multiplicity and coupling constants (*J*) were calculated automatically on MestReNova 10.0, NMR processing software from Mestrelab Research. The purity of the newly synthesized compounds as determined by analytical high-performance liquid chromatography (HPLC) was >95% on C-18 reversed-phase HPLC (Phenomenex, 10 mm × 250 mm) using an eluent of MeCN/H₂O = 60:40 at a flow rate of 3.0 mL/min. High-resolution mass spectrometry-electrospray ionization (HRMS-ESI) images were acquired on an

Agilent Q-TOF. UV absorption was measured on a Cary 50 Bio spectrophotometer using a standard 1 cm × 1 cm quartz cuvette. Fluorescence was measured with a Cary Eclipse spectrophotometer using a 1 cm × 1 cm quartz cuvette in a 10 mM MeCN solution.

tert-Butyl 4-((Diethoxyphosphoryl)methyl)phenylcarbamate (2). Compound 2 was synthesized according to our earlier published method.²³ To a 100 mL round-bottom flask with a magnetic stir bar, diethyl (4-aminobenzyl)phosphonate (1, 5.0 g, 20.56 mmol), di-*tert*-butyl dicarbonate (4.50 g, 21.0 mmol), tetrahydrofuran (THF, 25 mL), and water (10 mL) were added. The reaction mixture was stirred at room temperature open to air overnight. After completion of the reaction, THF was evaporated under vacuum and the resulting residue was diluted with water and extracted with ethyl acetate (EtOAc, 50 mL × 3). The organic layers were combined and washed with water (50 mL × 2) followed by brine (50 mL). The organic layer was dried over magnesium sulfate (MgSO₄), filtered, and evaporated under reduced pressure. A white amorphous compound was obtained (6.5 g; yield, 95%) and used without further purification.²³ ¹H NMR (400 MHz, chloroform-*d*) δ 7.30 (br d, *J* = 8.4 Hz, 2H), 7.17–7.19 (m, 2H), 6.87 (br s, 1H), 4.04–3.91 (m, 4H), 3.07 (d, ²*J*_{H,P} = 21.2 Hz, 2H), 1.49 (s, 9H), 1.22 (td, ³*J*_{H,H} = 6.8 Hz, ⁴*J*_{H,P} = 0.4 Hz, 6H). ¹³C NMR (100 MHz, chloroform-*d*) δ 152.8, 137.4, 130.1, 125.5, 118.4, 80.3, 62.0, 32.9 (d, ¹*J*_{C,P} = 138 Hz, 1C), 28.8, 16.3.

tert-Butyl 4-((Diethoxyphosphoryl)methyl)phenyl(5-fluoropentyl)carbamate (3). To a 100 mL round-bottom flask purged with argon gas and fitted with a magnetic stirrer were added sodium hydride (NaH, 0.174 g, 4.37 mmol, 60%) and *tert*-butyl 4-((diethoxyphosphoryl)methyl)phenylcarbamate (2, 0.50 g, 1.46 mmol). The mixture was purged with argon gas, and dry dimethylformamide (DMF, 4 mL) at 0 °C was added. To the reaction mixture, 1-bromo-5-fluoropentane (0.4 g, 2.91 mmol, *d* = 1.31 g/mL) was added dropwise after 30 min at 0 °C under argon gas. The reaction was stirred under argon and allowed to reach room temperature overnight. After completion, the reaction was quenched with water. The residue was dissolved in EtOAc and the aqueous layer was extracted with EtOAc (30 mL × 3). The organic layers were combined and washed with water (50 mL × 2) and brine (50 mL). The organic layer was dried over MgSO₄ and then filtered and concentrated to yield the desired product (3) as a sticky oil. This was purified over a silica flash column using 30% EtOAc in hexane as eluent, which resulted in the pure compound (0.55 g; yield, 43%). ¹H NMR (400 MHz, chloroform-*d*) δ 7.29 (d, *J* = 2.6 Hz, 1H), 7.27–7.26 (m, 1H), 7.11 (d, *J* = 8.0 Hz, 2H), 4.47 (t, *J* = 6.1 Hz, 1H), 4.36 (t, *J* = 6.1 Hz, 1H), 4.07–3.95 (m, 4H), 3.67–3.58 (m, 2H), 3.15 (d, ²*J*_{H,P} = 21.2 Hz, 2H), 1.76–1.61 (m, 4H), 1.57 (q, *J* = 7.3 Hz, 2H), 1.41 (s, 9H), 1.26–1.22 (m, 6H). ¹³C NMR (101 MHz, chloroform-*d*) δ 141.4, 130.4, 130.3, 129.5, 127.4, 84.9, 83.3, 80.3, 62.4, 62.32, 49.8, 34.2, 32.8 (d, ¹*J*_{C,P} = 138 Hz, 1C), 30.3, 30.1, 28.5, 28.5, 28.2, 22.6, 22.5, 16.6, 16.5. ¹⁹F NMR (376 MHz, chloroform-*d*) δ –86.02, –100.01.

General Method for the Synthesis of 4a–f (Scheme 1). To a 100 mL round-bottom flask purged with argon and fitted with a magnetic stirrer was added sodium hydride (2.0 equiv, 60% dispersion in mineral oil). The flask was purged with argon, and 2.0 mL of dry DMF was added. The compound (3, 1.1 equiv) was dissolved in dry DMF (2.0 mL) and transferred via syringe in a NaH–DMF mixture to a flask. The mixture was stirred under argon at 0 °C for 1 h. Commercially procured *para*-benzaldehyde (a–f, 1.0 equiv) was dissolved in dry DMF (2.0 mL) and added to the reaction mixture via a syringe under argon at 0 °C. The reaction mixture was stirred for 3 h at 0 °C in the dark under argon. The reactions were quenched with water and some of the derivatives precipitated out as an amorphous solid, which was filtered under vacuum and washed three to four times with water (50 mL each). Some of the compounds were extracted with EtOAc (30 mL × 3). The organic layers were combined and washed with water (25 mL × 2) followed by brine (25 mL). The organic layer was dried over MgSO₄, filtered, and evaporated under reduced pressure to yield the crude products. These were purified by dissolving in a minimal amount of dichloromethane (DCM) and made into a slurry with silica gel and then dried under vacuum. The compound was eluted with 10–15% EtOAc in hexane in a flash column.

tert-Butyl (E)-(5-Fluoropentyl)(4-(4-nitrostyryl)phenyl)carbamate (4a and 4b). The yellow sticky oil was purified in 10% EtOAc/hexane, yielding 0.25 g (79%). ¹H NMR (400 MHz, chloroform-*d*) δ 8.22 (d, *J* = 8.5 Hz, 2H), 7.63 (d, *J* = 8.8 Hz, 2H), 7.52 (d, *J* = 8.6 Hz, 2H), 7.28–7.21 (m, 3H), 7.11 (d, *J* = 15.2 Hz, 1H), 4.54–4.45 (m, 1H), 4.41–4.33 (m, 1H), 3.67 (t, *J* = 7.4 Hz, 2H), 1.77–1.52 (m, 6H), 1.45 (s, 9H). ¹³C NMR (101 MHz, chloroform-*d*) δ 168.3, 154.7, 144.0, 143.1, 133.9, 132.7, 127.5, 127.3, 127.0, 126.4, 124.4, 84.9, 83.3, 80.6, 49.8, 30.3, 30.1, 28.5, 28.3, 22.6, 22.6. ¹⁹F NMR (376 MHz, chloroform-*d*) δ –85.16 to –86.41 (m), –100.01.

tert-Butyl (E)-(5-Fluoropentyl)(4-(4-(methylamino)styryl)phenyl)carbamate (4c). The light yellow precipitate (ppt.) was obtained after water quenching and washing with water three times (20 mL each) and hexane once (20 mL), then dried under vacuum, yielding 0.080 g (46%). ¹H NMR (400 MHz, chloroform-*d*) δ 7.42 (d, *J* = 8.1 Hz, 2H), 7.36 (d, *J* = 8.2 Hz, 2H), 7.12 (d, *J* = 8.0 Hz, 2H), 7.00 (d, *J* = 16.2 Hz, 1H), 6.88 (d, *J* = 16.1 Hz, 1H), 6.60 (d, *J* = 8.2 Hz, 2H), 4.47 (t, *J* = 6.1 Hz, 1H), 4.35 (t, *J* = 6.1 Hz, 1H), 3.64 (t, *J* = 7.5 Hz, 2H), 2.87 (s, 3H), 1.68 (dd, *J* = 24.9, 7.4 Hz, 4H), 1.57–1.51 (m, 2H), 1.43 (s, 9H). ¹³C NMR (101 MHz, chloroform-*d*) δ 149.2, 141.1, 136.1, 136.1, 129.1, 127.9, 127.3, 126.4, 123.8, 112.6, 85.0, 80.3, 49.8, 30.8, 30.3, 30.1, 28.5, 28.2, 22.6. ¹⁹F NMR (376 MHz, chloroform-*d*) δ –100.01.

tert-Butyl (E)-(5-Fluoropentyl)(4-(4-(methylthio)styryl)phenyl)carbamate (4d). The white ppt. was obtained after water quenching, washed with water three times (20 mL each), and dried under vacuum, yielding 0.20 g (63%). ¹H NMR (400 MHz, chloroform-*d*) δ 7.46 (d, *J* = 8.5 Hz, 2H), 7.43 (d, *J* = 8.4 Hz, 2H), 7.24 (d, *J* = 8.4 Hz, 2H), 7.16 (d, *J* = 8.1 Hz, 2H), 7.03 (d, *J* = 1.5 Hz, 2H), 4.47 (t, *J* = 6.1 Hz, 1H), 4.36 (t, *J* = 6.1 Hz, 1H), 3.68–3.62 (m, 2H), 2.51 (s, 3H), 1.76–1.55 (m, 6H), 1.44 (s, 9H). ¹³C NMR (101 MHz, chloroform-*d*) δ 154.5, 141.5, 137.7, 134.8, 134.0, 127.8, 127.1, 126.9, 126.7, 126.5, 94.2, 84.6, 82.9, 80.0, 49.4, 30.0, 29.8, 28.2, 27.9, 22.2, 22.2, 15.6. ¹⁹F NMR (376 MHz, chloroform-*d*) δ –84.26 to –88.06 (m), –100.01.

tert-Butyl (E)-(5-Fluoropentyl)(4-(4-methoxystyryl)phenyl)carbamate (4e). The white amorphous compound was obtained from a flash silica column in 10% EtOAc/hexane in a yield of 0.10 g (36%). ¹H NMR (400 MHz, chloroform-*d*) δ 7.46 (d, *J* = 1.9 Hz, 2H), 7.44 (d, *J* = 1.5 Hz, 2H), 7.15 (d, *J* = 8.1 Hz, 2H), 7.01 (s, 1H), 6.97 (s, 1H), 6.92–6.88 (m, 2H), 4.47 (t, *J* = 6.1 Hz, 1H), 4.36 (t, *J* = 6.1 Hz, 1H), 3.83 (s, 3H), 3.69–3.61 (m, 2H), 1.77–1.58 (m, 4H), 1.57 (d, *J* = 1.8 Hz, 2H), 1.43 (d, *J* = 2.9 Hz, 9H). ¹³C NMR (101 MHz, chloroform-*d*) δ 159.4, 154.8, 141.5, 135.5, 130.2, 128.4, 127.8, 127.5, 126.6, 125.0, 114.3, 84.9, 83.3, 80.3, 55.5, 49.8, 30.3, 30.1, 28.5, 28.2, 28.1, 22.5, 22.5. ¹⁹F NMR (376 MHz, chloroform-*d*) δ –85.01 to –86.81 (m), –100.01.

tert-Butyl (E)-(5-Fluoropentyl)(4-(4-methylstyryl)phenyl)carbamate (4f). The white precipitate was obtained after water quenching and washing with water three times under vacuum (20 mL each); this compound was dried under high vacuum, yielding 0.25 g (83%). ¹H NMR (500 MHz, chloroform-*d*) δ 7.46 (d, *J* = 8.1 Hz, 2H), 7.41 (d, *J* = 7.8 Hz, 2H), 7.16 (t, *J* = 7.1 Hz, 4H), 7.04 (s, 2H), 4.46 (t, *J* = 6.1 Hz, 1H), 4.37 (t, *J* = 6.1 Hz, 1H), 3.65 (t, *J* = 7.4 Hz, 2H), 2.36 (s, 3H), 1.69 (dt, *J* = 25.2, 7.5 Hz, 2H), 1.61–1.51 (m, 4H), 1.43 (s, 9H). ¹³C NMR (126 MHz, chloroform-*d*) δ 154.8, 141.7, 137.7, 135.3, 134.6, 129.5, 128.8, 127.3, 127.1, 126.8, 126.5, 84.7, 83.4, 80.3, 49.8, 30.3, 30.1, 28.5, 28.2, 28.1, 22.5, 22.5, 21.4. ¹⁹F NMR (376 MHz, chloroform-*d*) δ –85.01 to –86.81 (m), –100.01.

General Method for Boc-Deprotection and Reduction (5a–f). In a 100 mL round-bottom flask fitted with a stir bar, compounds 4a–f were dissolved in EtOAc (15 mL) and methanol (10 mL). Stannous chloride (SnCl₂, 10 equiv)/hydrochloric acid (HCl, 1.2 M, 2 mL) was added to the solution. The mixture was fitted with a water condenser and heated to 70 °C for 6 h open to air in the dark. The reactions were monitored through thin-layer chromatography (TLC); after completion, the solvent was removed under vacuum. The residue was quenched by aqueous sodium bicarbonate (NaHCO₃, 20%) until bubbles stopped forming. Some of the compounds were precipitated and filtered under vacuum and washed with water three to four times (50 mL each). The other compounds were extracted in EtOAc (30 mL × 3) and washed with aqueous NaHCO₃ (20%, 30 mL × 2) and once

with water (50 mL) followed by brine (50 mL). It was then dried over MgSO_4 and the solvent was evaporated under reduced pressure. The crude product was dissolved in a minimal DCM slurry on silica and purified on silica by flash column chromatography using 10–15% EtOAc in hexane.²²

(E)-4-(4-Aminostyryl)-N-(5-fluoropentyl)aniline (5a). The yellow amorphous compound was eluted from a silica flash column using 10% EtOAc/hexane, yield 0.080 g (45%). ^1H NMR (400 MHz, chloroform-*d*) δ 7.30 (t, J = 8.5 Hz, 4H), 6.83 (d, J = 2.2 Hz, 2H), 6.66 (d, J = 8.5 Hz, 2H), 6.58 (d, J = 8.6 Hz, 2H), 4.53 (t, J = 6.0 Hz, 1H), 4.41 (t, J = 6.0 Hz, 1H), 3.71 (s, 2H), 3.16 (t, J = 7.0 Hz, 2H), 1.77 (d, J = 8.0 Hz, 1H), 1.77–1.63 (m, 4H), 1.61–1.49 (m, 3H). ^{13}C NMR (101 MHz, chloroform-*d*) δ 147.7, 145.5, 129.1, 127.6, 127.5, 127.4, 125.6, 124.7, 115.5, 113.0, 85.0, 83.4, 44.0, 30.5, 30.3, 29.4, 23.1, 23.1. ^{19}F NMR (376 MHz, chloroform-*d*) δ –85.52 to –86.41 (m), –100.01. HRMS (ESI+) calcd for ($\text{C}_{19}\text{H}_{23}\text{FN}_2$) [$\text{M} + \text{H}$]⁺ 299.1918, found 299.1919. HPLC purity: 99.99%, retention time: 9.53 min.

(E)-N-(5-Fluoropentyl)-4-(4-nitrostyryl)aniline (5b). The orange precipitate was obtained after quenching, in a yield of 0.080 g (65%). ^1H NMR (400 MHz, chloroform-*d*) δ 8.18 (d, J = 8.8 Hz, 2H), 7.55 (d, J = 8.8 Hz, 2H), 7.39 (d, J = 8.5 Hz, 2H), 7.19 (d, J = 16.2 Hz, 1H), 6.91 (d, J = 16.2 Hz, 1H), 6.60 (d, J = 8.6 Hz, 2H), 4.54 (t, J = 5.9 Hz, 1H), 4.42 (t, J = 5.9 Hz, 1H), 3.90 (s, 1H), 3.19 (t, J = 7.0 Hz, 2H), 1.83–1.65 (m, 4H), 1.59–1.51 (m, 3H). ^{13}C NMR (101 MHz, chloroform-*d*) δ 148.8, 144.8, 133.5, 128.4, 125.9, 125.1, 124.0, 121.4, 112.4, 84.6, 82.9, 43.3, 30.1, 29.9, 28.9, 22.8, 22.7. ^{19}F NMR (376 MHz, chloroform-*d*) δ –85.01 to –86.96 (m), –100.01. HRMS (ESI+) calcd for ($\text{C}_{19}\text{H}_{21}\text{FN}_2\text{O}_2$) [$\text{M} + \text{H}$]⁺ 329.1660, found 329.1662. HPLC purity: 95.36%, retention time: 7.52 min.

(E)-N-(5-Fluoropentyl)-4-(4-(methylamino)styryl)aniline (5c). The white amorphous compound was obtained from a silica flash column in 15% EtOAc/hexane in a yield of 0.030 g (60%). ^1H NMR (400 MHz, chloroform-*d*) δ 7.34 (s, 1H), 7.32 (d, J = 2.9 Hz, 2H), 7.30 (s, 1H), 6.83 (s, 2H), 6.60 (s, 1H), 6.58 (d, J = 3.6 Hz, 2H), 6.57 (s, 1H), 4.53 (t, J = 6.0 Hz, 1H), 4.41 (t, J = 6.0 Hz, 1H), 3.16 (t, J = 7.0 Hz, 2H), 2.86 (s, 3H), 1.77 (s, 1H), 1.74–1.64 (m, 3H), 1.59–1.54 (m, 1H), 1.52 (d, J = 6.6 Hz, 1H). ^{13}C NMR (101 MHz, chloroform-*d*) δ 148.6, 147.5, 127.8, 127.4, 127.3, 125.0, 113.0, 112.7, 84.9, 83.3, 44.0, 31.0, 30.5, 30.3, 29.4, 23.1, 23.1. ^{19}F NMR (376 MHz, chloroform-*d*) δ –85.16 to –86.61 (m), –100.01. HRMS (ESI+) calcd for ($\text{C}_{20}\text{H}_{25}\text{FN}_2$) [$\text{M} + \text{H}$]⁺ 313.2075, found 313.2076. HPLC purity: 95.48%, retention time: 10.90 min.

(E)-N-(5-Fluoropentyl)-4-(4-(methylthio)styryl)aniline (5d). The off-brown amorphous precipitate was formed by washing with water four times (50 mL each), yielding 0.125 g (81%). ^1H NMR (400 MHz, chloroform-*d*) δ 7.42 (d, J = 7.9 Hz, 2H), 7.40–7.32 (m, 4H), 7.18 (d, J = 7.7 Hz, 2H), 6.97 (d, J = 2.3 Hz, 2H), 4.45 (t, J = 6.0 Hz, 1H), 4.33 (t, J = 5.9 Hz, 1H), 3.24 (t, J = 8.0 Hz, 2H), 2.50 (s, 3H), 1.87 (s, 2H), 1.76–1.56 (m, 3H), 1.54–1.42 (m, 2H). ^{13}C NMR (101 MHz, chloroform-*d*) δ 138.6, 133.8, 129.3, 127.8, 127.1, 126.7, 126.5, 122.01, 83.7 (d, J = 164.9 Hz), 51.4, 30.1, 29.9, 26.0, 22.7, 22.7, 15.8. ^{19}F NMR (376 MHz, chloroform-*d*) δ –86.41 (td, J = 47.6, 23.9 Hz), –100.01. HRMS (ESI+) calcd for ($\text{C}_{20}\text{H}_{24}\text{FNS}$) [$\text{M} + \text{H}$]⁺ 330.1686, found 330.1692. HPLC purity: 97.58%, retention time: 7.20 min.

(E)-N-(5-Fluoropentyl)-4-(4-methoxystyryl)aniline (5e). The off pink ppt. was obtained, washed four times with water (50 mL each) under vacuum, and dried under high vacuum, yielding 0.070 g (92%). ^1H NMR (400 MHz, chloroform-*d*) δ 7.44 (s, 1H), 7.43–7.38 (m, 2H), 7.35 (d, J = 8.4 Hz, 2H), 6.92–6.84 (m, 4H), 6.77 (d, J = 8.1 Hz, 2H), 4.50 (d, J = 6.1 Hz, 1H), 4.38 (d, J = 6.1 Hz, 1H), 3.82 (s, 3H), 3.18 (t, J = 7.3 Hz, 2H), 1.71 (dt, J = 13.3, 6.1 Hz, 5H), 1.52 (t, J = 7.1 Hz, 3H). ^{13}C NMR (101 MHz, chloroform-*d*) δ 130.8, 127.9, 127.6, 127.5, 127.3, 126.7, 126.5, 115.2, 114.3, 114.3, 84.0 (d, J = 164.3 Hz), 55.5, 30.4, 30.2, 28.5, 23.0, 23. ^{19}F NMR (376 MHz, chloroform-*d*) δ –84.26 to –88.25 (m), –100.01. HRMS (ESI+) calcd for ($\text{C}_{20}\text{H}_{24}\text{FNO}$) [$\text{M} + \text{H}$]⁺ 314.1915, found 314.1918. HPLC purity: 97.58%, retention time: 7.20 min.

(E)-N-(5-Fluoropentyl)-4-(4-methylstyryl)aniline (5f). The white amorphous ppt. was obtained after water washing and dried under high vacuum, yielding 0.10 g (55%). ^1H NMR (400 MHz,

chloroform-*d*) δ 7.35 (t, J = 8.3 Hz, 4H), 7.13 (d, J = 7.8 Hz, 2H), 6.98 (d, J = 16.3 Hz, 1H), 6.87 (d, J = 16.3 Hz, 1H), 6.60 (d, J = 8.2 Hz, 2H), 4.53 (t, J = 6.0 Hz, 1H), 4.41 (t, J = 6.0 Hz, 1H), 3.16 (t, J = 7.0 Hz, 2H), 2.34 (s, 3H), 1.84–1.63 (m, 5H), 1.54 (q, J = 8.0 Hz, 3H). ^{13}C NMR (126 MHz, chloroform-*d*) δ 147.7, 136.7, 135.4, 129.4, 127.9, 127.7, 127.3, 126.1, 124.6, 113.1, 84.1 (d, J = 164.6 Hz), 44.1, 30.4, 30.3, 29.8, 29.2, 23.1, 23.03 21.3. ^{19}F NMR (376 MHz, chloroform-*d*) δ –84.62 to –87.35 (m), –100.01. HRMS (ESI+) calcd for ($\text{C}_{20}\text{H}_{24}\text{FN}$) [$\text{M} + \text{H}$]⁺ 298.1966, found 298.1970. HPLC purity: 94.85%, retention time: 8.25 min.

Synthesis of Pentane-1,5-diyl Bis(4-methylbenzenesulfonate) (7). To a 100 mL round-bottom flask with a magnetic stir bar charged with 4-methylbenzenesulfonyl chloride (2.29 g, 12.0 mmol) was added 25 mL of dry DCM as solvent, followed by trimethylamine (4.0 mL, 28.80 mmol). The solution was stirred for 30 min at room temperature and cooled to 0 °C. After 1 h at 0 °C, 1,5-diol-pentane (0.50 g, 4.80 mmol) was added and the reaction mixture was stirred overnight and warmed to room temperature. The reaction was monitored via TLC, and after completion of the reaction, the solvent was removed under reduced pressure, quenched with water, and extracted with EtOAc (50 mL \times 3). The combined organic layer was again washed with water (50 mL \times 2) followed by brine (50 mL). The organic layer was dried over MgSO_4 and evaporated under reduced pressure. The residue was dissolved in DCM/hexane (3:7) and kept at –10 °C for 4 h to yield a white crystallized compound in a yield of 1.30 g (65%). ^1H NMR (500 MHz, chloroform-*d*) δ 7.77 (d, J = 8.0 Hz, 4H), 7.35 (d, J = 7.9 Hz, 4H), 3.97 (t, J = 6.3 Hz, 4H), 2.46 (s, 6H), 1.67–1.56 (m, 4H), 1.42–1.31 (m, 2H). ^{13}C NMR (126 MHz, chloroform-*d*) δ 145.0, 133.1, 130.0, 128.0, 70.1, 28.3, 21.8, 21.6.

5-((tert-Butoxycarbonyl)(4-((diethoxyphosphoryl)methyl)phenyl)amino)pentyl 4-methylbenzenesulfonate (8). To a 100 mL round-bottom flask purged with argon and fitted with a stir bar was added sodium hydride (0.238 g, 6.00 mmol, 60%) and *tert*-butyl 4-((diethoxyphosphoryl)methyl)phenylcarbamate (2, 1.0 g, 2.91 mmol). The mixture was purged with argon, and dry DMF (5 mL) at 0 °C was added. Pentane-1,5-diyl bis(4-methylbenzenesulfonate) (7, 1.10 g, 2.65 mmol) was added after 30 min at 0 °C under argon. The reaction was stirred under argon and allowed to reach room temperature overnight. After completion, the reaction was quenched with water. The residue was dissolved in EtOAc and water, and the aqueous layer was extracted with EtOAc (30 mL \times 3). The organic layers were combined and washed with water (50 mL \times 2) followed by brine (50 mL). The organic layer was dried over MgSO_4 , then filtered and concentrated under vacuum to yield the desired product 3 as a sticky oil. This was purified over a silica flash column using 50% EtOAc in hexane as eluent to get the desired compound as an oil in a yield of 0.50 g (32%). ^1H NMR (500 MHz, chloroform-*d*) δ 7.76 (d, J = 8.3 Hz, 2H), 7.33 (d, J = 8.0 Hz, 2H), 7.25 (d, J = 2.6 Hz, 2H), 7.08 (d, J = 8.0 Hz, 2H), 4.06–3.96 (m, 6H), 3.54 (t, J = 7.4 Hz, 2H), 3.13 (d, $J_{\text{P-H}}$ = 21.6 Hz, 2H), 2.44 (s, 3H), 1.47 (p, J = 9.2, 7.8 Hz, 3H), 1.38 (s, 9H), 1.33–1.26 (m, 3H), 1.23 (t, J = 7.1 Hz, 6H). ^{13}C NMR (126 MHz, chloroform-*d*) δ 154.8, 144.8, 141.3, 141.3, 133.3, 130.3, 130.3, 130.0, 129.6, 129.5, 128.0, 127.3, 80.2, 70.5, 62.3, 62.3, 33.4 (d, $J_{\text{C,P}}$ = 138.4 Hz, 1C), 28.7, 28.5, 28.4, 27.9, 22.7, 21.8, 16.5, 16.5.

(E)-5-((tert-Butoxycarbonyl) (4-(4-Nitrostyryl)phenyl)amino)pentyl 4-Methylbenzene-sulfonate (9a). To a 100 mL round-bottom flask purged with argon and fitted with a magnetic stirrer were added sodium hydride (0.137 g, 3.43 mmol 60%) and 5-((tert-butoxycarbonyl)(4-((diethoxyphosphoryl)methyl)phenyl)amino)pentyl 4-methylbenzenesulfonate (8, 1.0 g, 1.71 mmol). The mixture was purged with argon, and dry DMF (4 mL) at 0 °C was added. 4-Nitrobenzaldehyde (0.260 g, 1.71 mmol) was dissolved in 2 mL of dry DMF and added dropwise in the reaction mixture after 30 min at 0 °C under argon. After 3 h, the reaction was monitored with TLC. On completion, the reaction was quenched with water and the solution was dissolved in EtOAc and water; the aqueous layer was extracted with EtOAc (30 mL \times 3). The organic layers were combined and washed with water (50 mL \times 2) followed by brine (50 mL). The organic layer was dried over MgSO_4 , then filtered and concentrated to yield the desired product (9a) as a sticky oil. This was purified over a silica flash

column using 15% EtOAc in hexane as eluent, forming a yellow amorphous compound in a yield of 0.40 g (40%). ^1H NMR (400 MHz, chloroform-*d*) δ 8.24 (d, J = 8.8 Hz, 2H), 7.78 (dd, J = 8.4, 1.8 Hz, 2H), 7.67–7.61 (m, 2H), 7.55–7.49 (m, 2H), 7.39–7.32 (m, 2H), 7.25–7.19 (m, 2H), 7.11 (dd, J = 16.3, 6.4 Hz, 1H), 4.05–3.98 (m, 2H), 3.63 (t, J = 7.4 Hz, 2H), 2.47 (s, 3H), 1.70–1.60 (m, 4H), 1.57–1.49 (m, 2H), 1.44 (s, 9H), 1.35 (q, J = 7.8 Hz, 2H). ^{13}C NMR (101 MHz, chloroform-*d*) δ 146.9, 145.1, 144.9, 144.0, 132.7, 130.1, 130.0, 128.1, 127.6, 127.5, 127.3, 127.0, 126.4, 124.4, 70.5, 70.2, 49.6, 28.7, 28.5, 28.4, 22.8, 21.9, 21.7.

Animal Preparation and Studies. All animal studies were performed in accordance with a guideline protocol approved by the Institutional Animal Care and Use Committee of Case Western Reserve University (Protocol 2016-0023, 2016-0028). The animals were treated with care to have minimal stress during tail vein injections. Wild-type C57BL/6 mice (6–8 weeks old, Jackson Laboratory, Bar Harbor, MN) were used for all in vitro and ex vivo tissue staining, and SD rats (Harlan Laboratories, Indianapolis, IN) were used for microPET/CT studies. The rats were fasted overnight prior to imaging but had access to water. Their diet was then resumed after microPET/CT imaging.

In Vitro Tissue Staining and Assay of Fluorescent Intensity. Wild-type mice (20–22 g, 8 weeks old) were deeply anesthetized and perfused transcardially with precooled saline (4 °C, 10 mL/min for 1 min, followed by 7 mL/min for 6 min). This was followed by fixation with precooled 4% PFA in PBS (4 °C, 10 mL/min for 1 min, followed by 7 mL/min for 6 min). Brain tissues were then removed, post-fixed by immersion in 4% PFA overnight, dehydrated in 10, 20, and 30% sucrose solution, embedded in a freezing compound at optimum cutting temperature (OCT, Fisher Scientific, Suwanee, GA), and sectioned at 20 μm with a cryostat (Thermo HMs25, Thermo Fisher Scientific Inc., Chicago, IL). Brain sections were collected from AP (1.0) to AP (−0.1)³³ and were mounted in 12 sections in order at the bottom of 12 superfrost slides (Fisher Scientific) with one section on each slide. Sections 13–24 were mounted in order in the middle of each slide, and sections 25–36 were mounted in order on the top of each slide. The sections were then incubated with test compounds (1 mM, 5% dimethyl sulfoxide (DMSO) in 1× PBS (pH 7.0), six sections per compound) for 25 min at room temperature in the dark. Excess compounds were washed by briefly rinsing the slides in PBS (1×) and coverslipped with Fluoromount-G mounting media (Vector Laboratories, Burlingame, CA). The sections were then examined under a microscope (Leica DM4000B, Leica Microsystems Inc., Buffalo Grove, IL) equipped with fluorescence (DFC7000T), and images of the stained mouse whole brain sections were taken with the same exposure time.

ImageJ software was then used to quantify pixel intensity values on six sections of each tested compound. White matter ROIs were selected on the genu of the corpus callosum (gcc, white matter), and the same-size ROI was applied to the gray matter on the midline between gcc and the edge of the section (Figure 4A). The images were analyzed by two experienced imaging scientists. The FIRs of white matter to gray matter were then calculated.

Ex Vivo Imaging. Wild-type mice were administered with the newly synthesized compounds (5a and 5c) (40 mg/kg) via tail vein injection, and 30 min later, the mice were perfused transcardially with saline followed by 4% PFA in PBS. Brain tissues were then removed, post-fixed by immersion in 4% PFA overnight, dehydrated in 30% sucrose solution, cryostat-sectioned at 100 μm , and mounted on superfrost slides, and images were acquired directly using a Leica fluorescence microscope.

Brain Focal Demyelination and in Vitro Staining Treated with LPC in a Rat Model. Sprague-Dawley female rats (n = 3, 200–220 g, 6–8 weeks old) were anesthetized by a freshly prepared mixture of ketamine and xylazine and positioned in a stereotaxic frame (Stoelting). A small incision was made in the scalp around the region of the corpus callosum using the following stereotaxic coordinates relative to the bregma: anterior–posterior, 0.0 mm; medial lateral, 2.0; and dorsal–ventral, 3.4. A small hole was drilled in the skull and a 26S-gauge needle attached to a 10 μL Hamilton syringe was lowered into the corpus callosum according to the dorsal–ventral coordinates. A microinjector pump (Stoelting) was used to control the infusion of 6

μL lysophosphatidylcholine (LPC, 0.1% in saline) at a rate of 0.25 $\mu\text{L}/\text{min}$. After infusion, the used needle was left in place for another 2 min to prevent fluid reflux out of the brain parenchyma. The incision was then closed via 5-0 Ethicon sutures, and the animals were allowed to recover on a heating pad. The animals were used for the study after 1 week of recovery. The treated rats were anesthetized and perfused with saline by 4% PFA. Brain tissues were removed, post-fixed in 4% PFA, dehydrated in 10, 20, and 30% sucrose solution, and embedded in OCT. The brain tissues were sectioned at 20 μm intervals with a cryostat. To determine if the selected test compound can differentiate demyelinated regions from normal myelinated sheaths, we conducted in vitro tissue staining using brain sections taken from LPC-treated rats. LPC-treated brain sections were then incubated with test compound 5a (1 mM, 5% DMSO in 1× PBS, pH 7.0) for 25 min at room temperature in the mounting media (Vector Laboratories, Burlingame, CA). The sections were examined under a microscope (Leica DM4000B, Leica Microsystems Inc., Buffalo Grove, IL) equipped with fluorescence (DFC7000T), and images of stained rat whole brain sections were acquired with the same exposure times. For the comparative study, standard luxol fast blue (LFB) staining was performed in the meantime on the adjacent LPC-treated brain tissue sections.

Rat SCI Model. Sprague-Dawley female rats (n = 3, 220–250 g, 8 weeks old) were anesthetized by a freshly prepared mixture of ketamine and xylazine, and a restricted laminectomy was conducted to expose the dorsal surface of T13. The vertebral column between T12 and L1 was then stabilized with clamps and forceps fixed to the base of an Infinite Horizon Impact Device. The midpoint of T13 was impacted with a force of 250 kdyn using a 2.5 mm stainless steel impactor tip, which was used to induce a moderately severe contusive injury to the spinal cord. The musculature was then sutured over the laminectomy site and the skin was closed with wound clips, followed by subsequent treatment with Marcaine at the incision site. The force/displacement graph was used to monitor impact consistency. After surgery, the animals were carefully monitored daily for pain and body weight with manual bladder expression two to three times daily to stimulate reflex voiding until the animals could urinate independently.

Image Processing for 3D Fluorescence and PET/CT Comparison. To confirm in vivo imaging of spinal cord white matter by PET/CT, we acquired two-dimensional (2D) fluorescence images and generated a 3D reconstructed image stack. Fluorescence images were acquired with a Leica fluorescent microscope and digitized using an in-built camera with RGB exposure of (R) 210 ms, (G) 2.5 ms, and (B) 1.0 ms. Light from a UV bulb source passed through an excitation filter (360 nm) and was collected after passing through an emission filter (400 nm). After extracting the spinal cord and removing the vertebral bone, sequential cuts were made with 100 μm slice thickness by a microtome. An image was captured for each slice and numbered according to the slice number, giving a series of 2D microscopic images along the length of the spine. The slices were sequentially aligned using a semiautomated image registration algorithm. Starting from the image of the first slice, the current slice was used as the reference image for alignment and the next slice then became the floating image, which was aligned via control point pairs between corresponding anatomic features in the two images. A 2D rigid-body transformation (translation, rotation) was used to transform the floating image to align with the reference and a minimum of three control point pairs were used for the transformation. Once two slices were aligned, the algorithm continued with the newly aligned image serving as the reference image and the next slice in the sequence served as the floating image. All the slices in the sequence were aligned by this technique to yield a 3D reconstructed fluorescence image volume (Figure 10). Image volumes from fluorescence, PET, and CT were visualized in Amira using volume-rendering and aligned based on the shape of the spine and fiducials from the vertebrae (Figure 9).

Radiosynthesis. No carrier-added [^{18}F] sodium fluoride was produced with a cyclotron (Eclipse High Production, Siemens) via the nuclear reaction ^{18}O (p,n) ^{18}F . At the end of bombardment, the activity of aqueous [^{18}F]fluoride ion (50–100 mCi) was transferred to a GE TRACERlab FXn synthesizer by high-pressure helium.

The radioactive solution was then passed through a Sep-Pak light QMA cartridge (Waters, WAT023525) that had been preconditioned with 5 mL of water, followed by 10 mL of air in a syringe. The radioactive solution was then eluted with K_2CO_3 solution (6 mg, 0.043 mmol, in 0.6 mL water), followed by K_{222} solution (12 mg, 0.032 mmol, in 1 mL acetonitrile). The solvent was evaporated under a stream of helium at 85 °C for 5 min, and the residue was subjected to vacuum at 55 °C for another 3 min to get the anhydrous $K_{222}/[^{18}F]$ fluoride ion complex. A solution of the tosylated precursors (3–5 mg, 0.0062–0.011 mmol, in 0.8 mL MeCN) was added to this dried complex, and the mixture was heated at 110 °C for 10 min. EtOAc (3 mL) and hexane (2 mL) were added to the reaction vessel and the mixture was passed through a preconditioned Sep-Pak silica cartridge (Waters, WAT020520; preconditioned with 5 mL of ether). The solvent was removed under a stream of helium at 70 °C, and the residue was added to a tin chloride solution (30 mg, 0.16 mmol in 1 mL ethanol and 0.5 mL HCl (1 M)). The resulting mixture was heated at 115 °C for 10–20 min. NaOH solution (0.8 mL, 1 M) and water (15 mL) were then added, and the resulting mixture was passed through a preconditioned Sep-Pak C-18 cartridge (Waters, WAT020515 preconditioned with 5 mL of ethanol, followed by 10 mL of water, then dried by 10 mL of air in a syringe). The cartridge was washed with another 20 mL of water, and the crude products were eluted with 1 mL of acetonitrile, which was further purified by semipreparative HPLC (Phenomenex C-18, 10 mm \times 250 mm, MeCN/ H_2O (60:40), flow rate = 5 mL/min, t_R = 9 min). The radioactive fraction containing the desired products was collected, diluted with water, loaded onto a Sep-Pak C-18 cartridge, and eluted with 1 mL of ethanol. After evaporation, the residue was redissolved in 5% ethanol in saline solution and filtered (0.22 μ m) into a sterile injection bottle for animal use. The total time of radiosynthesis was 70 min. Radiochemical purity (RCP) and molar activity (A_m) were determined by analytical HPLC (Phenomenex C-18, 4.6 mm \times 250 mm, MeCN/ H_2O (65:35), flow rate = 1 mL/min, t_R = 6–10 min). Specific activity was calculated by the area of the UV peak of purified F-18 compound and titrated with the standard curve of the non-radioactive reference compound of known concentration.

MicroPET/CT Image Acquisition and Analysis. MicroPET/CT imaging was performed using a Siemens Inveon microPET/CT scanner in the Case Center for Imaging Research. For better anatomic localization, CT co-registration was applied. Before microPET imaging, CT scout views were taken to ensure that the brain tissues were placed in the co-scan field of view, where the highest image resolution and sensitivity are achieved. Anesthesia was induced with isoflurane (2–5% in oxygen). Under anesthesia, radiotracer (1–2 mCi, 37–74 MBq) was administered via tail vein injection and immediately followed by a dynamic PET acquisition up to 60 min. Once microPET acquisition was done, the rat was moved into the CT field and a two-bed CT scan was performed. A two-dimensional ordered subset expectation maximization algorithm was used for image reconstruction using CT for the attenuation correction. For quantitative analysis, the resultant PET images were registered to the CT images, which enabled us to accurately define the ROI and quantify the radioactivity concentrations. In this study, the whole brains of rodents were used as the ROIs and the radioactivity concentrations were determined in terms of SUV or % ID.

■ ASSOCIATED CONTENT

📄 Supporting Information

The Supporting Information is available free of charge on the ACS Publications website at DOI: [10.1021/acs.jmedchem.8b01354](https://doi.org/10.1021/acs.jmedchem.8b01354).

NMR, HPLC, and HRMS spectra (PDF)

■ AUTHOR INFORMATION

Corresponding Authors

*E-mail: cwx130@case.edu (C.W.).

*E-mail: ywx91@case.edu (Y.W.).

ORCID

Yanming Wang: [0000-0002-2886-2978](https://orcid.org/0000-0002-2886-2978)

Notes

The authors declare no competing financial interest.

■ ACKNOWLEDGMENTS

This work was supported in part by the National Multiple Sclerosis Society (RG5174 and PP1703-27324), Genzyme Corporation, Bryon Riesch Paralysis Foundation, and NIH (R21 NS111433).

■ ABBREVIATIONS

s, singlet; br s, broad singlet; dd, doublet of doublets; ddd, doublet of doublet of doublets; br d, broad doublets; t, triplet; dt, triplet of doublets; q, quartet; m, multiplet; br m, broad multiplet; NMR, nuclear magnetic resonance; MTR, magnetization transfer ratio; CIC, case imaging compound; BMB, myelin-binding agent; TAFDAS, triazole fluorinated diamino stilbene; MeDAS, methyl diamino stilbene; FC2MeDAS, (*E*)-4-(4-amino-3-(2-fluoroethoxy)styryl)-*N*-methylaniline; K_{222} , 4,7,13,16,21,24-hexaoxa-1,10-diazabicyclo[8.8.8]hexacosane; NaH, sodium hydride; $SnCl_2$, stannous chloride; K_2CO_3 , potassium carbonate; $MgSO_4$, magnesium sulfate; HCl, hydrochloric acid; THF, tetrahydrofuran; DMF, dimethylformamide; DCM, dichloromethane; EtOAc, ethyl acetate; NaOH, sodium hydroxide; TsCl, *p*-toluenesulfonyl chloride; MeCN, acetonitrile; EtOH, ethanol; SUV, standardized uptake value; ID, injected dose; ROI, region of interest; CT, computerized tomography; *d*, deuterated; PFA, paraformaldehyde; RCP, radiochemical purity; OCT, optimum cutting temperature; FIR, fluorescence intensity ratio; LPC, lysophosphatidylcholine; LFB, luxol fast blue; CNS, central nervous system; PET, positron emission tomography; SMP, small molecular probe; MRI, magnetic resonance imaging; HPLC, high-performance liquid chromatography

■ REFERENCES

- (1) Ju, G.; Wang, J.; Wang, Y.; Zhao, X. Spinal Cord Contusion. *Neural Regen. Res.* **2014**, *9*, 789–794.
- (2) Franklin, R. J. M.; Ffrench-Constant, C. Remyelination in the CNS: From Biology to Therapy. *Nat. Rev. Neurosci.* **2008**, *9*, 839–855.
- (3) Mei, F.; Fancy, S. P. J.; Shen, Y. A.; Niu, J.; Zhao, C.; Presley, B.; Miao, E.; Lee, S.; Mayoral, S. R.; Redmond, S. A.; Etxeberria, A.; Xiao, L.; Franklin, R. J. M.; Green, A.; Hauser, S. L.; Chan, J. R. Micropillar Arrays as a High-Throughput Screening Platform for Therapeutics in Multiple Sclerosis. *Nat. Med.* **2014**, *20*, 954–960.
- (4) Bai, L.; Lennon, D. P.; Caplan, A. I.; DeChant, A.; Hecker, J.; Kranso, J.; Zaremba, A.; Miller, R. H. Hepatocyte Growth Factor Mediates Mesenchymal Stem Cell-Induced Recovery in Multiple Sclerosis Models. *Nat. Neurosci.* **2012**, *15*, 862–870.
- (5) Mei, F.; Fancy, S. P.; Shen, Y. A.; Niu, J.; Zhao, C.; Presley, B.; Miao, E.; Lee, S.; Mayoral, S. R.; Redmond, S. A.; Etxeberria, A.; Xiao, L.; Franklin, R. J.; Green, A.; Hauser, S. L.; Chan, J. R. Micropillar Arrays as a High-Throughput Screening Platform for Therapeutics in Multiple Sclerosis. *Nat. Med.* **2014**, *20*, 954–960.
- (6) Cruz-Martinez, P.; Gonzalez-Granero, S.; Molina-Navarro, M. M.; Pacheco-Torres, J.; Garcia-Verdugo, J. M.; Geijo-Barrientos, E.; Jones, J.; Martinez, S. Intraventricular Injections of Mesenchymal Stem Cells Activate Endogenous Functional Remyelination in a Chronic Demyelinating Murine Model. *Cell Death Dis.* **2016**, *7*, No. e2223.
- (7) Mi, S.; Miller, R. H.; Tang, W.; Lee, X.; Hu, B.; Wu, W.; Zhang, Y.; Shields, C. B.; Zhang, Y.; Miklasz, S.; Shea, D.; Mason, J.; Franklin, R. J.; Ji, B.; Shao, Z.; Chedotal, A.; Bernard, F.; Roulois, A.; Xu, J.; Jung, V.; Pepinsky, B. Promotion of Central Nervous System Remyelination by

Induced Differentiation of Oligodendrocyte Precursor Cells. *Ann. Neurol.* **2009**, *65*, 304–315.

(8) Brugarolas, P.; Popko, B. Remyelination Therapy Goes to Trial for Multiple Sclerosis. *Neurol.: Neuroimmunol. Neuroinflammation* **2014**, *1*, No. e26.

(9) Chen, J. T.; Kuhlmann, T.; Jansen, G. H.; Collins, D. L.; Atkins, H. L.; Freedman, M. S.; O'Connor, P. W.; Arnold, D. L. Canadian MS/BMT Group. Voxel-Based Analysis of the Evolution of Magnetization Transfer Ratio to Quantify Remyelination and Demyelination with Histopathological Validation in a Multiple Sclerosis Lesion. *NeuroImage* **2007**, *36*, 1152–1158.

(10) Le Bihan, D.; Mangin, J.-F.; Poupon, C.; Clark, C. A.; Pappata, S.; Molko, N.; Chabriat, H. Diffusion Tensor Imaging: Concepts and Applications. *J. Magn. Reson. Imaging* **2001**, *13*, 534–546.

(11) Enzinger, C.; Fazekas, F. Measuring Gray Matter and White Matter Damage in MS: Why This is Not Enough. *Front. Neurol.* **2015**, *6*, No. 56.

(12) Vargas, W. S.; Monohan, E.; Pandya, S.; Raj, A.; Vartanian, T.; Nguyen, T. D.; Hurtado Rúa, S. M.; Gauthier, S. A. Measuring Longitudinal Myelin Water Fraction in New Multiple Sclerosis Lesions. *NeuroImage* **2015**, *9*, 369–375.

(13) Phelps, M. E. Positron Emission Tomography Provides Molecular Imaging of Biological Processes. *Proc. Natl. Acad. Sci. U.S.A.* **2000**, *97*, 9226–9233.

(14) Stankoff, B.; Wang, Y.; Bottlaender, M.; Aigrot, M. S.; Dolle, F.; Wu, C.; Feinstein, D.; Huang, G. F.; Semah, F.; Mathis, C. A.; Klunk, W.; Gould, R. M.; Lubetzki, C.; Zalc, B. Imaging of CNS Myelin by Positron-Emission Tomography. *Proc. Natl. Acad. Sci. U.S.A.* **2006**, *103*, 9304–9309.

(15) Wu, C.; Tian, D.; Feng, Y.; Polak, P.; Wei, J.; Sharp, A.; Stankoff, B.; Lubetzki, C.; Zalc, B.; Mufson, E. J.; Gould, R. M.; Feinstein, D. L.; Wang, Y. A Novel Fluorescent Probe That is Brain Permeable and Selectively Binds to Myelin. *J. Histochem. Cytochem.* **2006**, *54*, 997–1004.

(16) Wang, Y.; Wu, C.; Capriello, A. V.; Somoza, E.; Zhu, W.; Wang, C.; Miller, R. H. In Vivo Quantification of Myelin Changes in the Vertebrate Nervous System. *J. Neurosci.* **2009**, *29*, 14663–14669.

(17) Wang, C.; Popescu, D. C.; Wu, C.; Zhu, J.; Macklin, W.; Wang, Y. In Situ Fluorescence Imaging of Myelination. *J. Histochem. Cytochem.* **2010**, *58*, 611–621.

(18) Wu, C.; Wang, C.; Popescu, D. C.; Zhu, W.; Somoza, E. A.; Zhu, J.; Condie, A. G.; Flask, C. A.; Miller, R. H.; Macklin, W.; Wang, Y. A Novel PET Marker for In Vivo Quantification of Myelination. *Bioorg. Med. Chem.* **2010**, *18*, 8592–8599.

(19) Frullano, L.; Wang, C.; Miller, R. H.; Wang, Y. A Myelin-Specific Contrast Agent for Magnetic Resonance Imaging of Myelination. *J. Am. Chem. Soc.* **2011**, *133*, 1611–1613.

(20) Stankoff, B.; Freeman, L.; Aigrot, M. S.; Chardain, A.; Dolle, F.; Williams, A.; Galanaud, D.; Armand, L.; Lehericy, S.; Lubetzki, C.; Zalc, B.; Bottlaender, M. Imaging Central Nervous System Myelin by Positron Emission Tomography in Multiple Sclerosis Using [Methyl-(1)(1)C]-2-(4'-methylaminophenyl)-6-hydroxybenzothiazole. *Ann. Neurol.* **2011**, *69*, 673–680.

(21) Wang, C.; Wu, C.; Zhu, J.; Miller, R. H.; Wang, Y. Design, Synthesis, and Evaluation of Coumarin-Based Molecular Probes for Imaging of Myelination. *J. Med. Chem.* **2011**, *54*, 2331–2340.

(22) Condie, A. G.; Gerson, S. L.; Miller, R. H.; Wang, Y. Two-Photon Fluorescent Imaging of Myelination in the Spinal Cord. *ChemMedChem* **2012**, *7*, 2194–2203.

(23) Frullano, L.; Zhu, J.; Miller, R. H.; Wang, Y. Synthesis and Characterization of a Novel Gadolinium-Based Contrast Agent for Magnetic Resonance Imaging of Myelination. *J. Med. Chem.* **2013**, *56*, 1629–1640.

(24) de Paula Faria, D.; de Vries, E. F. J.; Sijbesma, J. W. A.; Dierckx, R. A. J. O.; Buchpiguel, C. A.; Copray, S. PET Imaging of Demyelination and Remyelination in the Cuprizone Mouse Model for Multiple Sclerosis: A Comparison Between [¹¹C]CIC and [¹¹C]MeDAS. *NeuroImage* **2014**, *87*, 395–402.

(25) de Paula Faria, D.; Copray, S.; Sijbesma, J. W. A.; Willemsen, A. T. M.; Buchpiguel, C. A.; Dierckx, R. A. J. O.; de Vries, E. F. PET Imaging of Focal Demyelination and Remyelination in a Rat Model of Multiple Sclerosis: Comparison of [¹¹C]Medas, [¹¹C]CIC and [¹¹C]PIB. *Eur. J. Nucl. Med. Mol. Imaging* **2014**, *41*, 995–1003.

(26) Wu, C.; Eck, B.; Zhang, S.; Zhu, J.; Tiwari, A. D.; Zhang, Y.; Zhu, Y.; Zhang, J.; Wang, B.; Wang, X.; Wang, X.; You, J.; Wang, J.; Guan, Y.; Liu, X.; Yu, X.; Trapp, B. D.; Miller, R.; Silver, J.; Wilson, D.; Wang, Y. Discovery of 1,2,3-Triazole Derivatives for Multimodality PET/CT/Cryoimaging of Myelination in the Central Nervous System. *J. Med. Chem.* **2017**, *60*, 987–999.

(27) Tiwari, A. D.; Wu, C.; Zhu, J.; Zhang, S.; Zhu, J.; Wang, W. R.; Zhang, J.; Tatsuoka, C.; Matthews, P. M.; Miller, R. H.; Wang, Y. Design, Synthesis and Evaluation of Fluorinated Radioligands for Myelin Imaging. *J. Med. Chem.* **2016**, *59*, 3705–3718.

(28) Wu, C.; Zhu, J.; Baeslack, J.; Zaremba, A.; Hecker, J.; Kraso, J.; Matthews, P. M.; Miller, R. H.; Wang, Y. Longitudinal Positron Emission Tomography Imaging for Monitoring Myelin Repair in the Spinal Cord. *Ann. Neurol.* **2013**, *74*, 688–698.

(29) Demirci, E.; Ahmed, R.; Ocak, M.; Latoche, J.; Radelet, A.; DeBlasio, N.; Mason, N. S.; Anderson, C. J.; Mountz, J. M. Preclinical Evaluation of (¹⁸F)-ML-10 to Determine Timing of Apoptotic Response to Chemotherapy in Solid Tumors. *Mol. Imaging* **2017**, *16*, No. 1536012116685941.

(30) Kim, J. W.; Seo, S.; Kim, H. S.; Kim, D. Y.; Lee, H. Y.; Kang, K. W.; Lee, D. S.; Bom, H. S.; Min, J. J.; Lee, J. S. Comparative Evaluation of the Algorithms for Parametric Mapping of the Novel Myocardial PET Imaging Agent (¹⁸F)-FPTP. *Ann. Nucl. Med.* **2017**, *31*, 469–479.

(31) Rotstein, B. H.; Wey, H. Y.; Shoup, T. M.; Wilson, A. A.; Liang, S. H.; Hooker, J. M.; Vasdev, N. PET Imaging of Fatty Acid Amide Hydrolase with [¹⁸F]DOPP in Nonhuman Primates. *Mol. Pharmacology* **2014**, *11*, 3832–3838.

(32) Parhi, A. K.; Wang, J. L.; Oya, S.; Choi, S.-R.; Kung, M.-P.; Kung, H. F. 2-(2'-((Dimethylamino)methyl)-4'-(fluoroalkoxy)-phenylthio)-benzenamine derivatives as Serotonin Transporter Imaging Agents. *J. Med. Chem.* **2007**, *50*, 6673–6684.

(33) Gegrge, P.; Watson, C. *The Rat Brain in Stereotaxic Coordinates*, 6th ed.; Elsevier Inc: London, U.K., 2007.